

Supplementary information

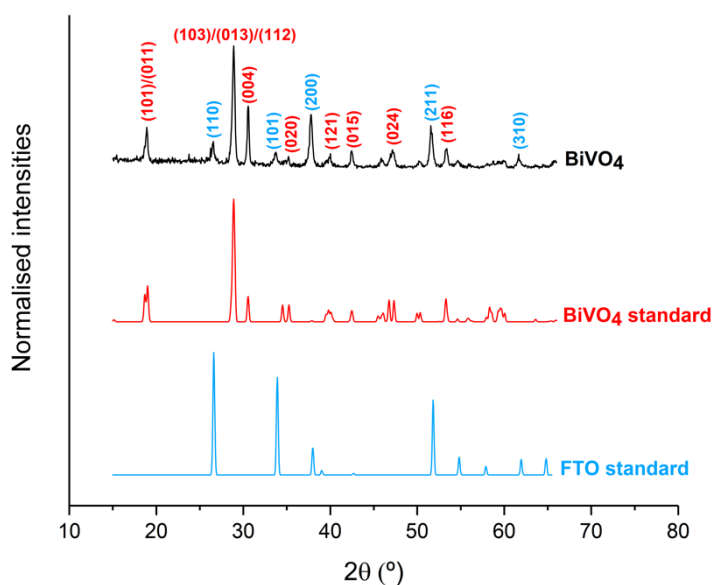


Fig. S1 BiVO₄ XRD pattern compared against BiVO₄ and FTO standards.

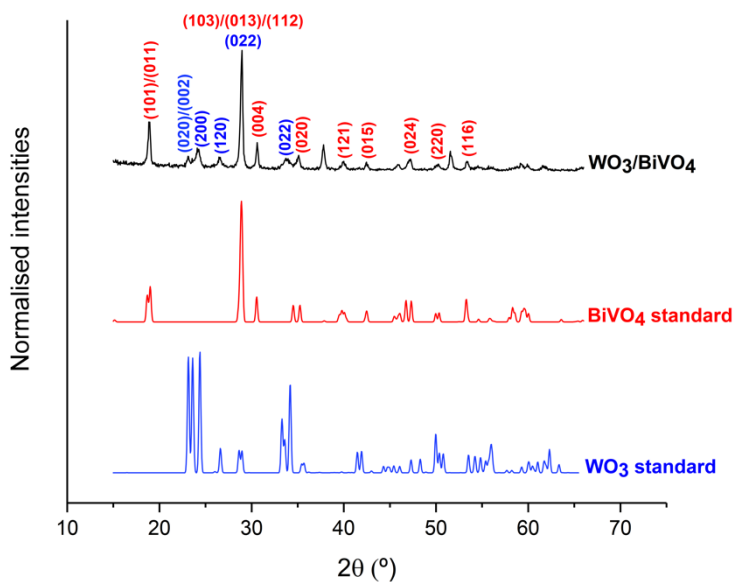


Fig. S2 WO₃/BiVO₄ heterojunction sample XRD pattern compared against BiVO₄ and WO₃ standards.

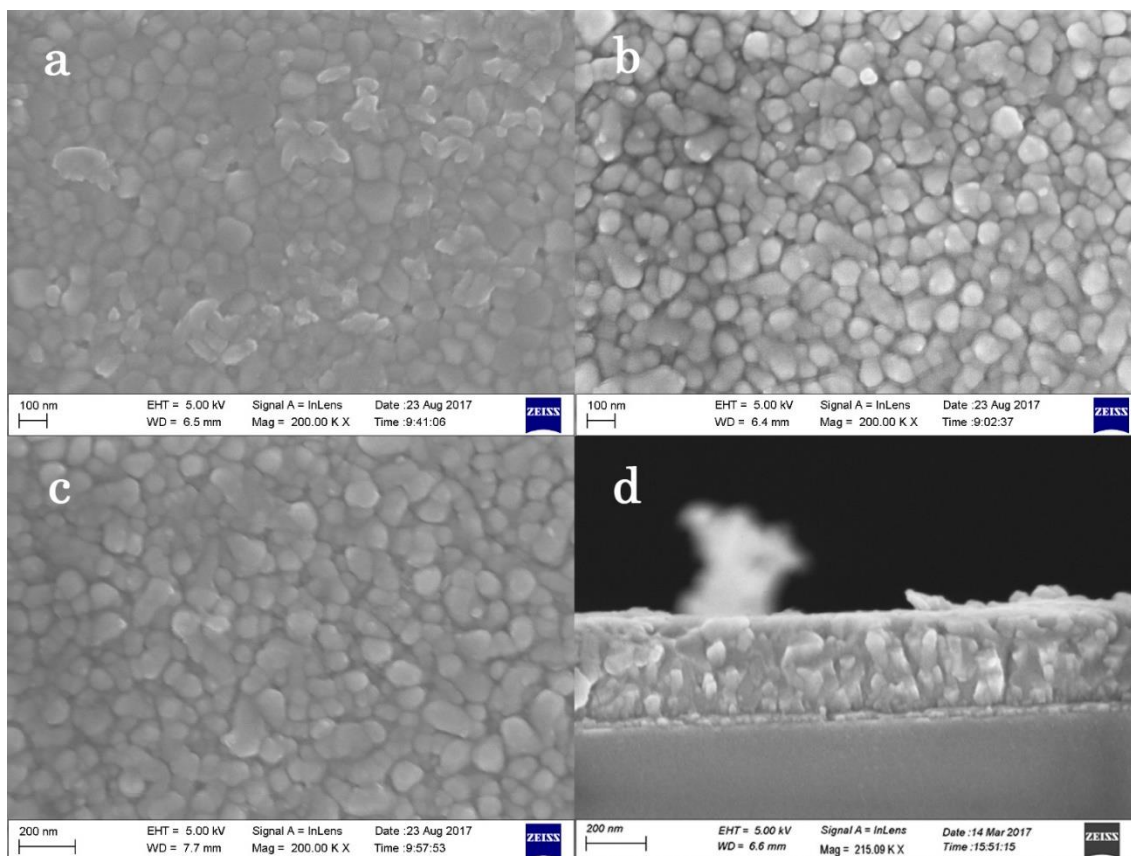


Fig. S3 SEM images of top view (a) BiVO₄, (b) WO₃/BiVO₄ and (c) WO₃ and (d) a cross section of a WO₃/BiVO₄ sample.

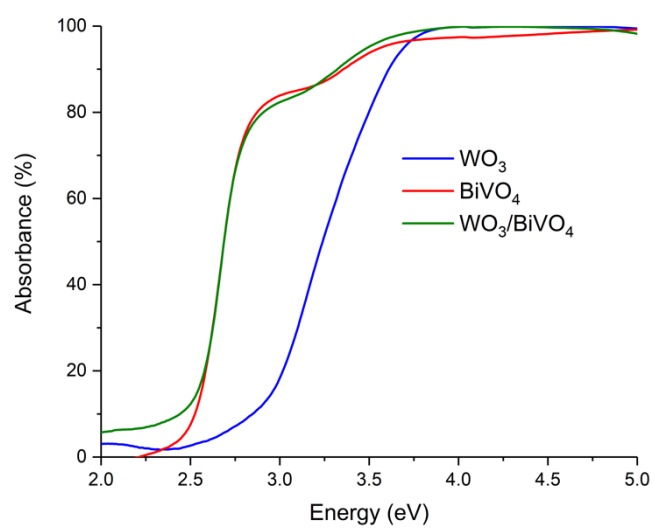


Fig. S4 UV-Visible absorption spectroscopy of all samples.

Absorption coefficient (α): $T = e^{-\alpha l} \Rightarrow \alpha = -\frac{\ln(T)}{l}$

where T is the transmittance fraction and l (nm) the material thickness.

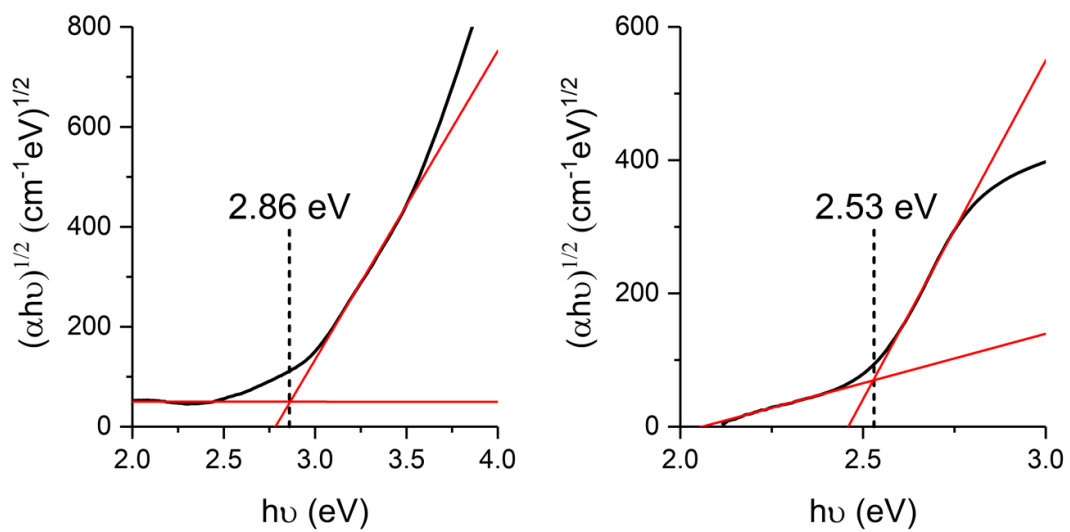


Fig. S5 Tauc plots for the determination of the indirect optical bandgap of WO_3 (left) and BiVO_4 (right).

Penetration depth (δ): $\delta = \frac{1}{\alpha}$

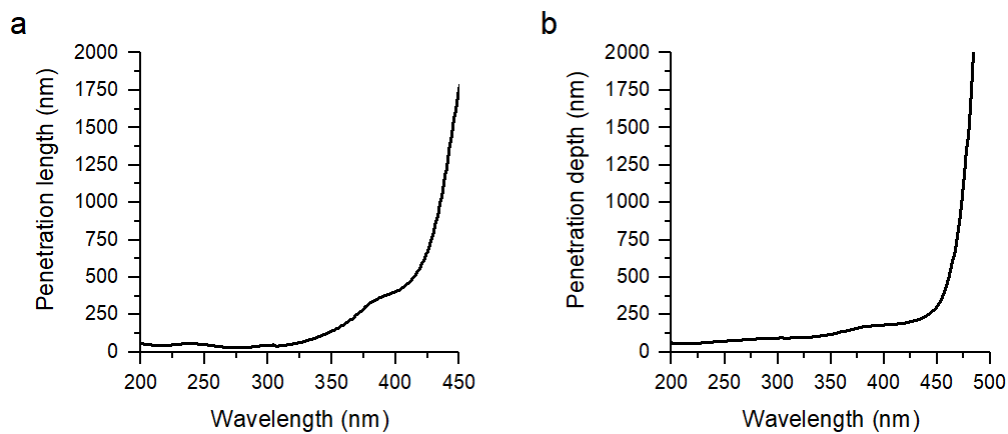


Fig. S6 Penetration depth vs wavelength for WO_3 (a) and BiVO_4 (b).

BiVO ₄	E _{FB} (V vs RHE)	N _D (cm ⁻³)
Hong et al. ¹	0.02	-
Yimeng et al. ²	0.1	10 ¹⁸
Sayama et al. ³	0.0±0.1	0.3·10 ¹⁸
Zhang et al. ⁴	0.1	-
Moniz et al. ⁵	0.05	-

WO ₃	E _{FB} (V vs RHE)	N _D (cm ⁻³)
Hong et al. ¹	0.41	8.1·10 ¹⁸
Kalanur et al. ⁶	0.924	2.3·10 ¹⁹
Radecka et al. ⁷	0.512	-
Castro et al. ⁸	0.25	1.17·10 ²⁰

Table S1 Literature values of flat band potential and donor densities for WO₃ and BiVO₄.

	E _{FB} (V vs RHE)	N _D	m _e	m _h
BiVO ₄	0.1	10 ¹⁸	0.9 ⁹	0.7 ⁹
WO ₃	0.5	10 ¹⁹	1.75 ¹⁰	1.75 ¹⁰

Table S2 Parameters used in the band bending model.

Band bending model

The valence band maximum (VBM), conduction band minimum (CBM) and Fermi level were calculated from parameters derived from our EIS experiments. The Fermi level can be estimated to be equal to the flat band potential, which can be related to energy vs vacuum through the absolute electrode potential conversion:

$$E_{NHE} = -E_{vacuum} - 4.44 V$$

Then, the Fermi level can be related to the conduction band edge through the following equation:¹¹

$$E_{F(FB)} - E_{CB} = k_B T \ln \left(\frac{N_D}{N_C} \right)$$

where $E_{F(FB)}$ is the Fermi level, E_{CB} CBM, k_B the Boltzmann constant, T the temperature, N_D the donor concentration and N_C the effective density of states in the conduction band, which can be calculated as a function of the electron effective mass as follows:¹¹

$$N_C = 2 \left(\frac{2\pi m_e^* k_B T}{h^2} \right)^{\frac{3}{2}}$$

Then, the VBM value can be obtained by subtracting the optical band gap from the CBM:

$$E_{VB} = E_{CB} - E_g$$

The band bending model of an isotype (n-n) heterojunction is formulated under two assumptions: (i) the band gap of each material remains constant throughout the junction and (ii) the Fermi level is constant at thermal equilibrium. A modified version of an ordinary p-n junction was used:¹²

$$\Delta E_F = E_F^{(1)} - E_F^{(2)}$$

$$V_o^{(1)} = \Delta E_F \left(\frac{N_D^{(2)} \epsilon_r^{(2)}}{N_D^{(2)} \epsilon_r^{(2)} + N_D^{(1)} \epsilon_r^{(1)}} \right) \quad V_o^{(2)} = \Delta E_F \left(\frac{N_D^{(1)} \epsilon_r^{(1)}}{N_D^{(1)} \epsilon_r^{(1)} + N_D^{(2)} \epsilon_r^{(2)}} \right)$$

$$x_N^{(1)} = \left(\frac{2\epsilon_r^{(1)} \epsilon_o V_o^{(1)}}{qN_D^{(1)}} \right)^{\frac{1}{2}} \quad x_N^{(2)} = \left(\frac{2\epsilon_r^{(2)} \epsilon_o V_o^{(2)}}{qN_D^{(2)}} \right)^{\frac{1}{2}}$$

$$E_V(x) \begin{cases} E_C^{(1)} - V_o & -\infty < x < -x_N \\ E_C^{(1)} - V_o^{(1)} + \frac{qN_D^{(1)} (x + x_N^{(1)})^2}{2\epsilon_r^{(1)} \epsilon_o} & x_N < x < 0 \\ E_C^{(2)} + V_o^{(2)} - \frac{qN_D^{(2)} (x - x_N^{(2)})^2}{2\epsilon_r^{(2)} \epsilon_o} & 0 < x < x_n \\ E_C^{(2)} + V_o & x_n < x < +\infty \end{cases}$$

$$E_F^{(eq)} = E_F^{(1)} - V_o^{(1)} = E_F^{(2)} + V_o^{(2)}$$

Computational results

	Fock mixing (%)	O basis set	a (Å)	b (Å)	c (Å)	β (°)	Band gap (eV)
		Experimental	7.30	7.54	7.69	90.88	2.86
B3LYP (20% HF)	20	8-411d1 (Harrison <i>et al</i> 1996)	7.47	7.74	7.95	90.05	3.00
	20	8-411 (Towler et al. 1994)	7.56	7.70	7.81	90.00	2.43
	20	8-411d1 (Bredow et al. 2006)	7.47	7.73	7.92	90.01	2.98
	10	8-411d1 (Bredow et al. 2006)	7.51	7.77	7.95	90.00	2.16
	20	8-411d1 (Cora et al. 2005)	7.45	7.74	7.93	90.12	3.06
	20	Wang et al. 2011	7.44	7.73	7.91	90.20	3.13
PBE0 (20% HF)	25	8-411d1 (Harrison <i>et al</i> 1996)	7.37	7.65	7.87	90.17	3.62
	25	8-411 (Towler et al. 1994)	7.51	7.64	7.74	90.00	2.79
	25	8-411d1 (Bredow et al. 2006)	7.35	7.62	7.81	90.38	3.59
	25	Wang et al. 2011	7.33	7.60	7.80	90.60	3.67
HSE06 (25% HF)	25	8-411d1 (Harrison <i>et al</i> 1996)	7.36	7.64	7.85	90.33	2.93
	25	8-411 (Towler et al. 1994)	7.52	7.64	7.73	90.00	2.09
	25	8-411d1 (Bredow et al. 2006)	7.36	7.61	7.82	90.36	2.89
	25	8-411d1 (Cora et al. 2005)	7.34	7.60	7.82	90.57	2.97
	25	Wang et al. 2011	7.39	7.64	7.75	90.30	2.80

Table S3 DFT calculations of the lattice parameters and band gap energies of γ -WO₃ for different combinations of functionals and oxygen basis sets. Experimental values (green) and literature values (blue) are also shown.

		Fock exchange (%)	O basis set	a (Å)	b (Å)	c (Å)	γ (°)	Band gap (eV)
			Experimental	5.19	5.11	11.70	90.3	2.53
B3LYP	20		8-411 (Towler et al. 1994)	5.23	5.12	11.65	90.61	3.5
	20		8-411d1 (Bredow et al. 2006)	5.30	5.07	11.99	90.91	3.81
	10		8-411d1 (Bredow et al. 2006)	5.29	5.09	11.97	90.58	2.92
	20		8-411d1 (Cora et al. 2005)	5.29	5.08	11.92	90.86	3.77
PBE0	25		8-411d1 (Harrison et al 1996)	5.17	5.04	11.65	90.35	3.91
	25		8-411 (Towler et al. 1994)	5.12	5.10	11.45	90.06	3.73
	25		8-411d1 (Bredow et al. 2006)	5.18	5.04	11.70	90.34	3.93
	25		8-411d1 (Cora et al. 2005)	5.17	5.04	11.65	90.29	3.90
HSE06	25		8-411d1 (Harrison et al 1996)	5.06	5.06	11.47	90.00	3.0
	25		8-411 (Towler et al. 1994)	5.11	5.11	11.44	90.01	3.06
	25		8-411d1 (Bredow et al. 2006)	5.26	5.09	11.82	90.30	3.0
	25		8-411d1 (Cora et al. 2005)	5.16	5.05	11.62	90.22	3.19

Table S4 DFT calculations of the lattice parameters and band gap energies of monoclinic BiVO_4 for different combinations of functionals and oxygen basis sets. Experimental values (green) and literature values (blue) are also shown.

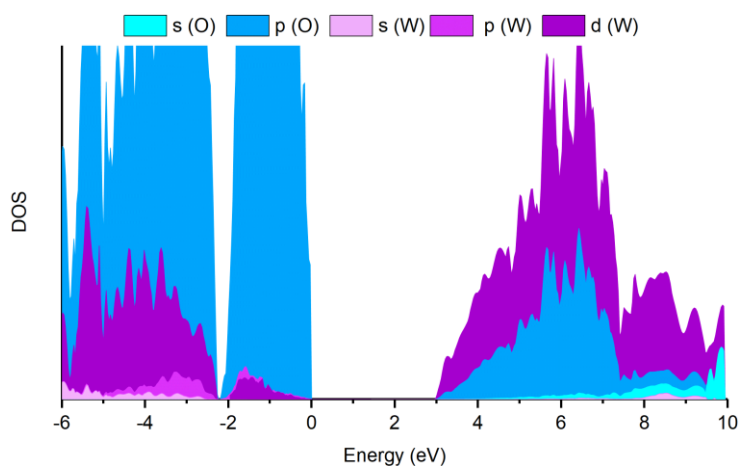


Fig. S7 γ - WO_3 PDOS derived from the relaxed crystal structure obtained using B3LYP (20% HF) and the oxygen basis set of Bredow et al.

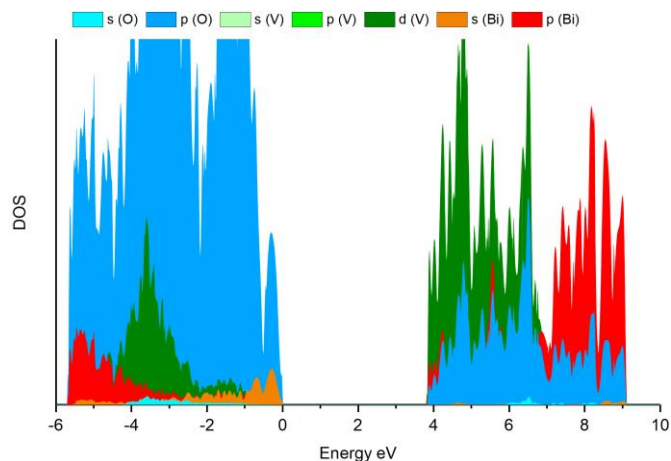


Fig. S8 Monoclinic BiVO₄ PDOS derived from the relaxed crystal structure obtained using B3LYP (20% HF) and the oxygen basis set of Bredow *et al.*

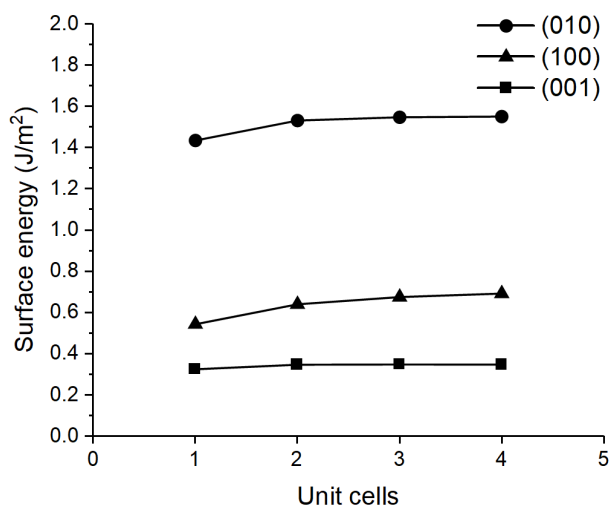


Fig. S9 Surface energy of the (010), (100) and (001) surfaces of γ -WO₃.

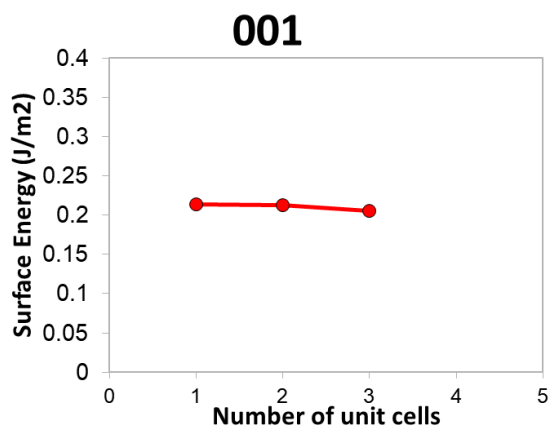


Fig. S10 Surface energy of the 001 surface of monoclinic BiVO₄.

Heterojunction modelling

When approaching the atomic structure between these two materials it is a good starting point to consider the most stable surfaces for both materials because these are the most predominant facets on the surface of a polycrystalline sample. For BiVO_4 , the (001) surface has been proved to be not only the preferred direction of growth for some synthesis methods but is also the one that has the least surface energy due to its low surface area.^{13,14} For WO_3 , the (001) surface is well known as an easy cleavage direction for the preparation of WO_3 single crystals due to an antiferroelectric distortion in the W sublattice that causes the layering of the crystal.^{15,16} The surface energy of this crystallographic direction have also been proven to be the most stable in γ -monoclinic WO_3 .¹⁷ Theoretically, the crystal can be cleaved in either the W plane or the O plane, however, WO_3 tends to lose the oxygens when cut in the O plane to cancel the electrostatic dipole. One way to achieve dipole neutrality is by a $(\sqrt{2} \times \sqrt{2})R45^\circ$ reconstruction where the crystal is cut through the O plane and then half of the oxygen monolayer is removed by taking out oxygens in alternate positions in both the [100] and [010] direction.¹⁸

Since the WO_3 (001) surface doesn't match well with any of the BiVO_4 low Miller index surfaces including the (001) (Fig. S6) a redefinition of BiVO_4 lattice vectors is necessary. A supercell of the (001) surface with lattice vectors $\vec{u} = \vec{a} + \vec{b}$ and $\vec{v} = -\vec{a} + \vec{b}$ coupled with a 45° cell rotation (Fig. 20). The resulting supercell will be an almost square ($\gamma=90.86^\circ$) $7.27 \times 7.31 \text{ \AA}^2$ cell which matches reasonably well the square $7.30 \times 7.54 \text{ \AA}^2$ WO_3 (001) unit cell.

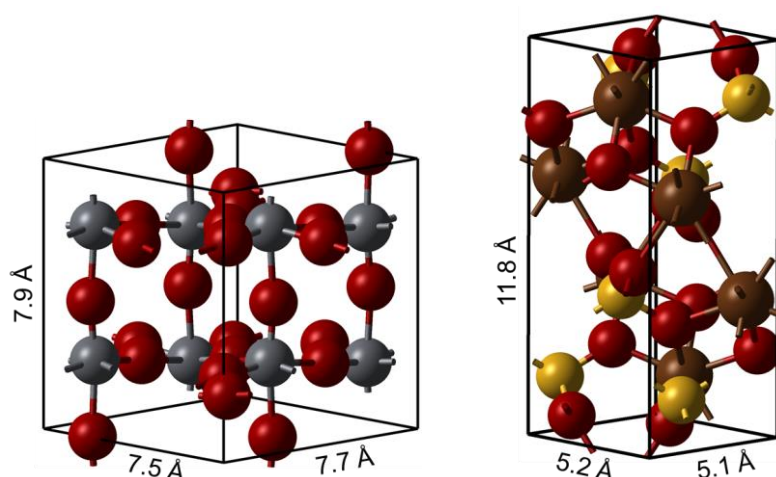


Fig. S11 Unit cells and lattice parameters of γ - WO_3 and monoclinic BiVO_4 . Colour code: oxygen (red), tungsten (grey), bismuth (brown) and vanadium (yellow).

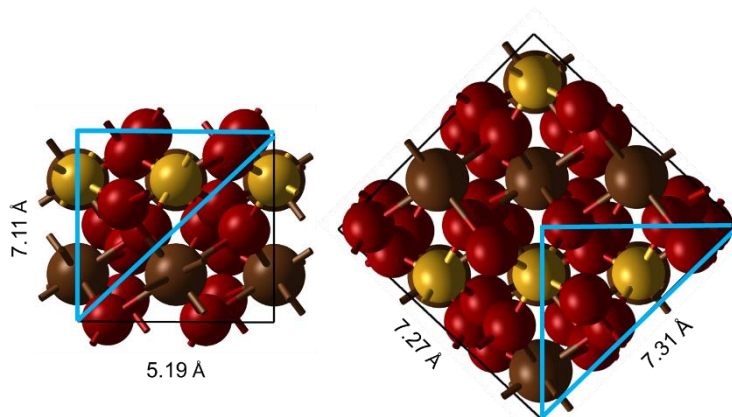


Fig. S12 Monoclinic BiVO_4 unit cell vs the supercell used in this work. Colour code: oxygen (red), bismuth (brown) and vanadium (yellow).

When modelling an interface between two materials it is important to look for atomic bonds that can connect both materials. In general, oxygen bonds constitute the standard bridging mechanism for metal oxides. Looking at the top view of both surfaces, there are two undercoordinated oxygens at the edge of the WO_3 (001) surface and 2 undercoordinated Bi atoms near the BiVO_4 (001) surface that present a complementary zig-zag pattern (Fig. S8). In addition, there are two W atoms that remain undercoordinated in the W plane near the surface whereas at the top of the BiVO_4 surface there are still 4 undercoordinated oxygens. The main connection points were identified to be the undercoordinated WO_3 oxygens with the undercoordinated BiVO_4 bismuths, thus, the unit cells were aligned accordingly. After geometry relaxation the undercoordinated tungsten atoms formed a bond with two of the four undercoordinated BiVO_4 oxygens after a rotation of the VO_4^{3-} tetrahedras closest to the interface (Fig. S9). Both of these oxygens break their bond with bismuth to bond with the undercoordinated tungsten atoms at the WO_3 side rendering the Bi atoms at the surface undercoordinated. Table S4 compares the bond distances in the VO_4^{3-} tetrahedras that are near the edge/interface for the heterojunction system, a BiVO_4 slab with the same lattice parameters as in the heterojunction and a BiVO_4 slab with bulk lattice parameters. Oxygens O2 and O6 are those closer to the edge and when the heterojunction is formed these will link the two materials together by bonding to the exposed W atoms in the WO_3 slab. The V1-O2 and the V2-O6 bonds shorten after the formation of the heterojunction. The small difference between the two BiVO_4 slab systems indicates that the strain caused by the BiVO_4 adapting to the WO_3 lattice upon the formation of the heterojunction is very minor.

Interface bonds	Heterojunction interface	Heterojunction bulk	BiVO4 slab edge with heterojunction lattice parameters	BiVO4 slab edge with bulk lattice parameters
V1-O1	1.6548	1.6153	1.5982	1.6196
V1-O2	1.6903	1.7772	1.7314	1.6741
V1-O3	1.7229	1.7858	1.7802	1.8278
V1-O4	1.8726	1.7873	1.8621	1.8379
V2-O5	1.6554	1.6163	1.5936	1.6198
V2-O6	1.6905	1.7771	1.7342	1.6733
V2-O7	1.7236	1.7811	1.8271	1.8285
V2-O8	1.8701	1.7872	1.8411	1.8379

Table S5 Comparison of bond distances in the VO_4^{3-} tetrahedras at the edge or interface in different systems.

Table S5 compares the bond distances in the WO_6 octahedras that are near the edge/interface for the heterojunction system and an isolated WO_3 slab with the same lattice parameters as in the bulk (which are the same as in the heterojunction system). The oxygens O2 and O8 are those closer to the edge and when the heterojunction is formed these will link the two materials together by bonding to the exposed Bi atoms in the BiVO_4 slab. There are no substantial differences between these systems which supports the idea that the BiVO_4 lattice adapts to the WO_3 lattice. Table S7 shows the average of the atomic charges calculated by Mulliken population analysis at the heterojunction interface and at the bulk of the individual components.

Interface bonds	Heterojunction interface	Heterojunction bulk	WO3 slab edge
W1-O1	1.7775	1.7592	1.6983
W1-O2	1.7824	1.7811	1.8127
W1-O3	1.8344	1.8663	1.9057
W1-O4	1.9809	1.9482	2.1261
W1-O5	2.1131	2.1162	2.2298
W1-O6	2.1294	2.2001	2.2720
W2-O7	1.7761	1.7595	1.6984
W2-O8	1.7788	1.7809	1.8130
W2-O9	1.8448	1.8659	1.9057
W2-O10	1.9679	1.9479	2.1261
W2-O11	2.1235	2.1186	2.2292
W2-O12	2.1392	2.1991	2.2717

Table S6 Comparison of bond distances in the WO_6 octahedras at the edge or interface in different systems.

	Interface	Bulk WO ₃	Bulk BiVO ₄
W	10.961	11.013	-
O	8.873	8.997	8.8545
Bi	83.594	-	83.523
V	21.176	-	21.058

Table S7 Averaged atomic charges at the heterojunction interface and at the bulk of the individual components.

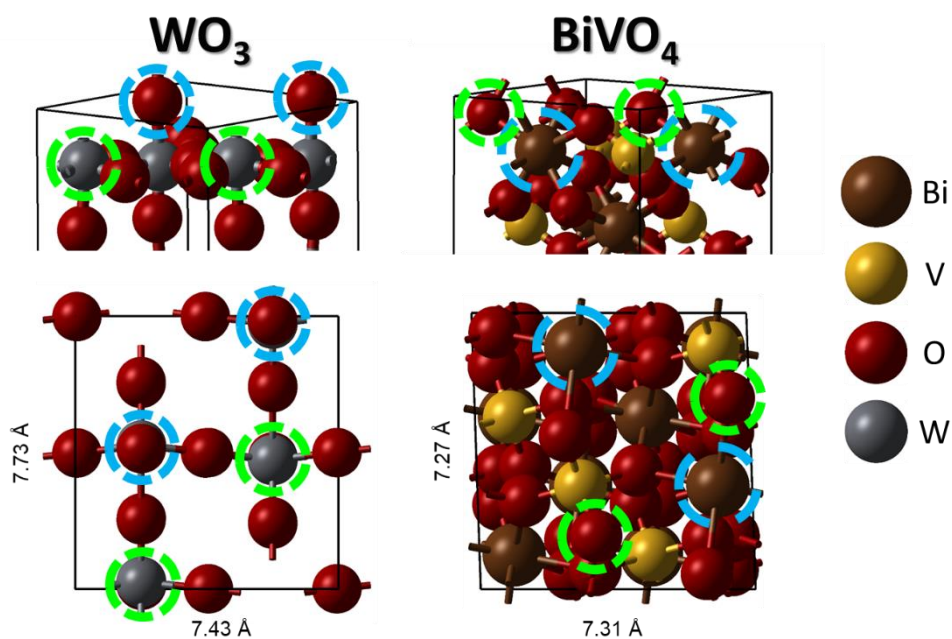


Fig. S13 Linking points between at the monoclinic BiVO₄ and γ -WO₃ interface. W-O-Bi bonds in blue and W-O-V bonds in green.

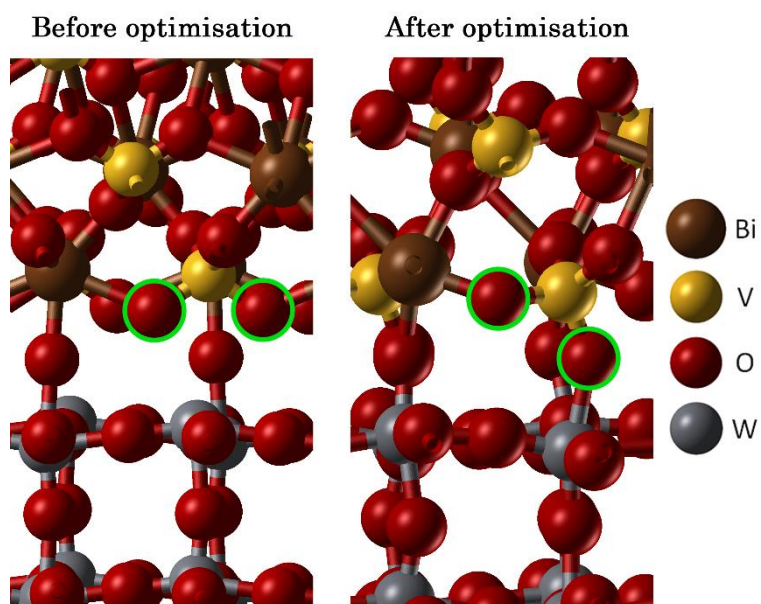


Fig. S14 Rotation of the VO₄³⁻ tetrahedra at the WO₃/BiVO₄ interface before and after geometry optimisation.

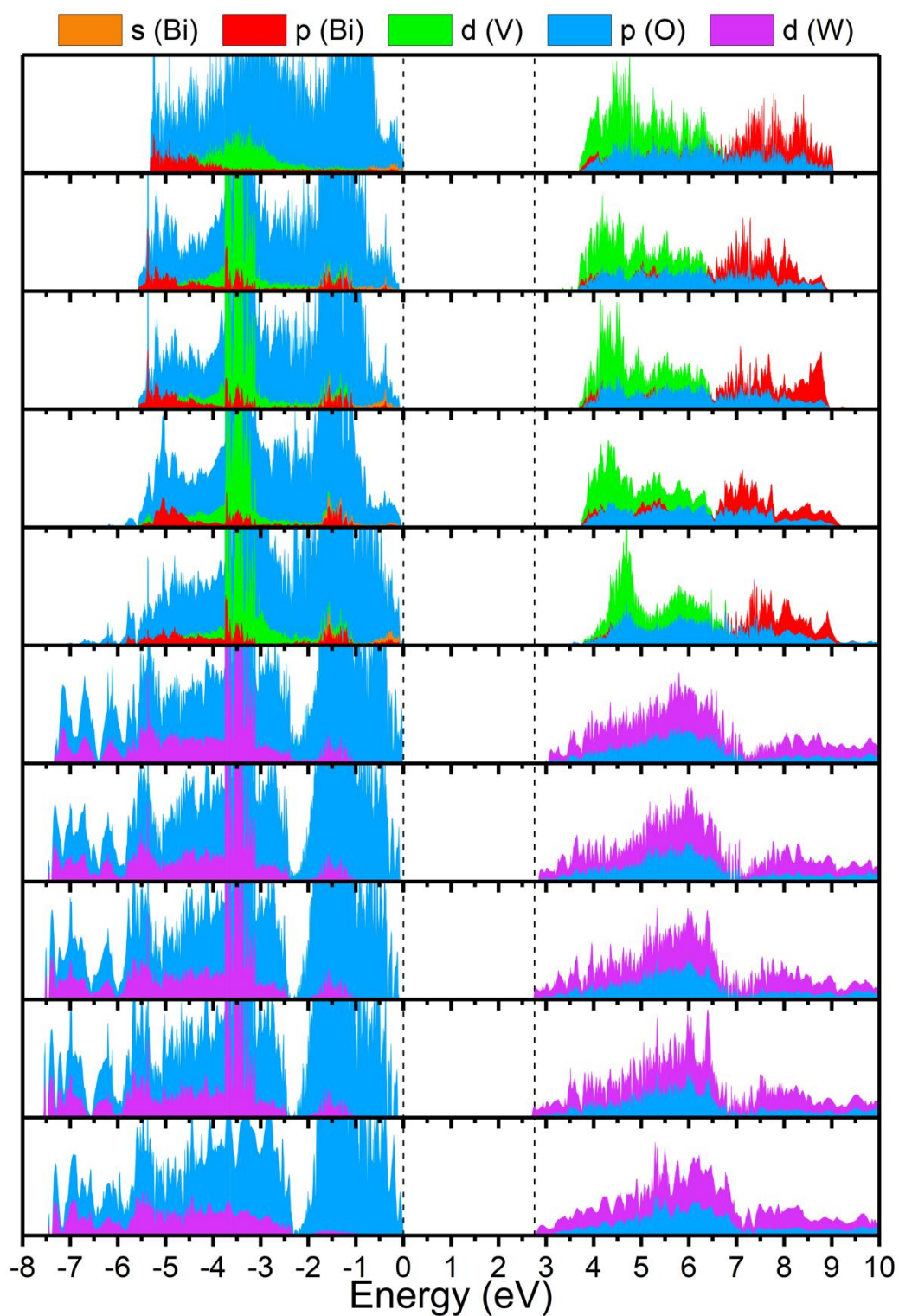


Fig. S15 Layer-by-layer projected density of states (LPDOS) across the heterojunction (8 middle graphs) and a PDOS of the central portion of a 3 unit cell BiVO₄ slab (top graph) and a 4 unit cell γ -WO₃ slab. The HSE06 hybrid functional was used to calculate the energy from the geometry obtained with B3LYP.

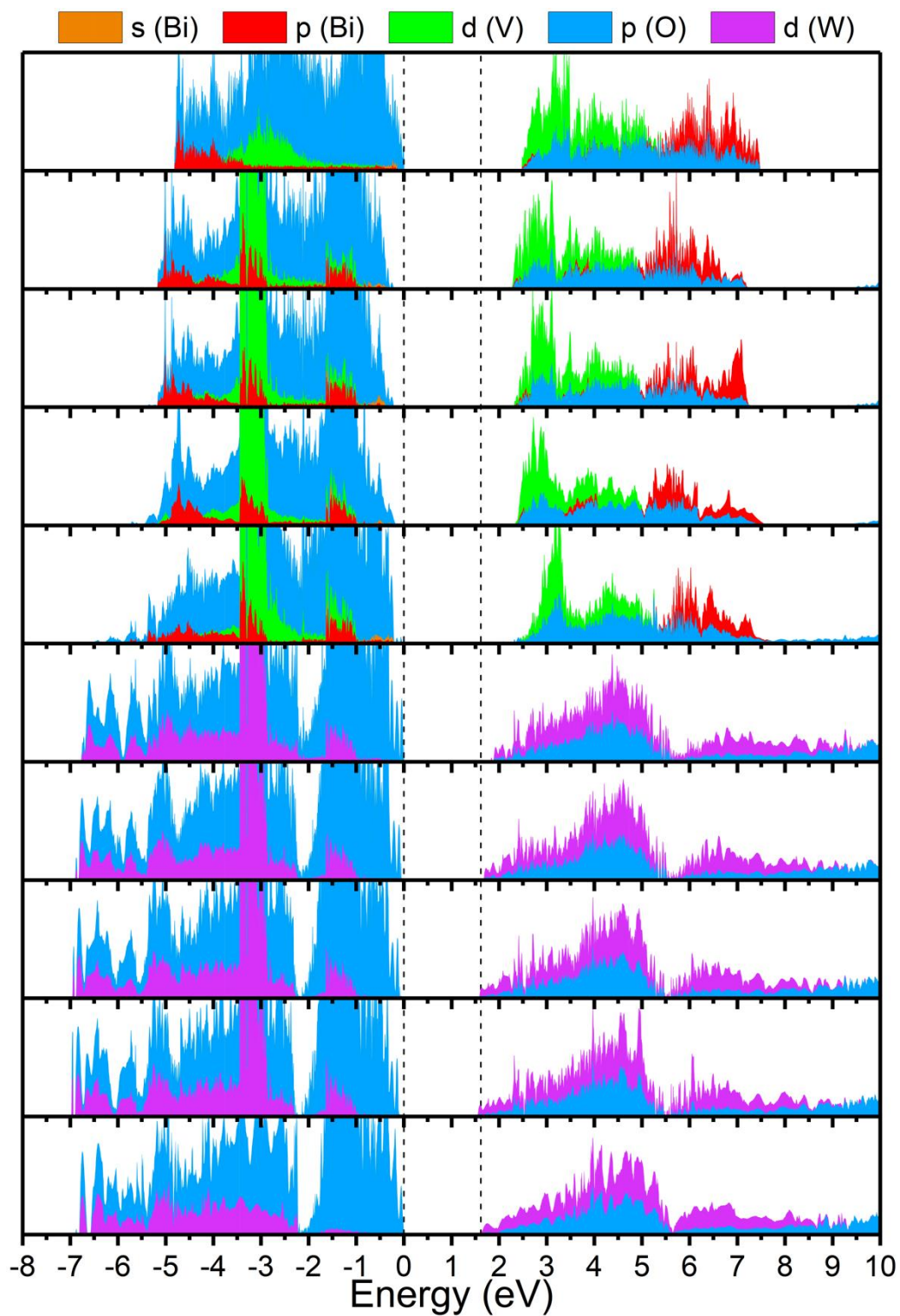


Fig. S16 Layer-by-layer projected density of states (LPDOS) across the heterojunction (8 middle graphs) and a PDOS of the centre portion of a 3 unit cell BiVO_4 slab (top graph) and a 4 unit cell $\gamma\text{-WO}_3$ slab. The PBE GGA functional was used to calculate the energy from the geometry obtained with B3LYP.

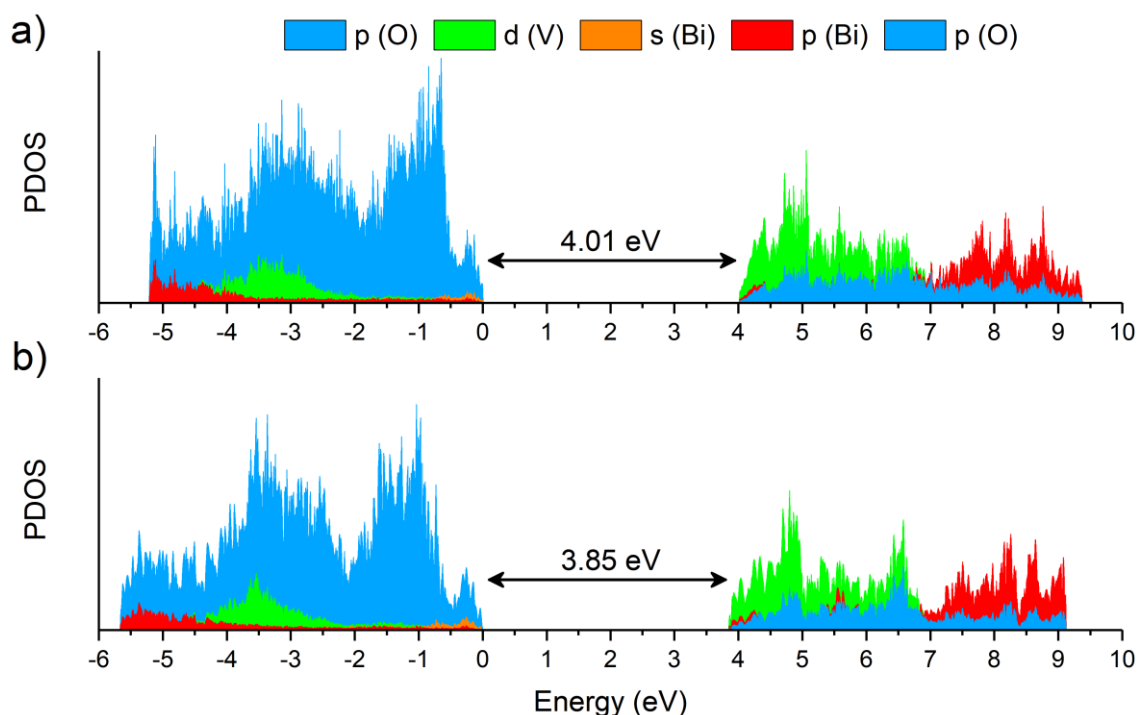


Fig. S17 Projected density of states of the central portion (bulk-like) of a BiVO₄ slab with the lattice parameters of the heterojunction (a) and the same slab with the lattice parameters of the bulk BiVO₄ (b). The B3LYP hybrid functional was used to relax the geometries and calculate the energy.

References

- (1) Hong, S. J.; Lee, S.; Jang, J. S.; Lee, J. S. *Energy Environ. Sci.* **2011**, *4* (5), 1781.
- (2) Ma, Y.; Pendlebury, S. R.; Reynal, A.; Le Formal, F.; Durrant, J. R.; Gratzel, M.; Durrant, J. R.; Klug, D. R.; Durrant, J. R.; Sunkara, M.; McFarland, E. W.; Domen, K.; Miller, E. L.; Turner, J. A.; Dinh, H. N. *Chem. Sci.* **2014**, *5* (8), 2964–2973.
- (3) Kazuhiro Sayama, *, †; Atsushi Nomura, ‡; Takeo Arai, †; Tsuyoshi Sugita, ‡; Ryu Abe, †; Masatoshi Yanagida, †; Takashi Oi, §; Yasukazu Iwasaki, §; Yoshimoto Abe, ‡ and; Sugihara†, H. **2006**.
- (4) Zhang, Y.; Yi, Z.; Wu, G.; Shen, Q. *J. Photochem. Photobiol. A Chem.* **2016**, *327*, 25–32.
- (5) Moniz, S. J. A.; Zhu, J.; Tang, J. *Adv. Energy Mater.* **2014**, *4* (10), 1301590.
- (6) Kalanur, S. S.; Yoo, I.-H.; Seo, H. *Electrochim. Acta* **2017**, *254*, 348–357.
- (7) Radecka, M.; Sobas, P.; Wierzbicka, M.; Rekas, M. *Phys. B Condens. Matter* **2005**, *364* (1–4), 85–92.
- (8) Castro, I. A.; Byzynski, G.; Dawson, M.; Ribeiro, C. J. *J. Photochem. Photobiol. A Chem.* **2017**, *339*, 95–102.
- (9) Zhao, Z.; Li, Z.; Zou, Z. *Phys. Chem. Chem. Phys.* **2011**, *13* (10), 4746–4753.

- (10) Berak, J. M.; Sienko, M. J. *J. Solid State Chem.* **1970**, *2* (1), 109–133.
- (11) Gurevich, Y. Y.; Pleskov, Y. V.; Rotenberg, Z. A. *Photoelectrochemistry*; Springer US: Boston, MA, 1980.
- (12) Sze, S. M.; Ng, K. K. *Physics of semiconductor devices*; Wiley-Interscience, 2007.
- (13) Xi, G.; Ye, J. *Chem. Commun.* **2010**, *46* (11), 1893.
- (14) Nasir, S. N. F. M.; Ullah, H.; Ebadi, M.; Tahir, A. A.; Sagu, J. S.; Mat Teridi, M. A. *J. Phys. Chem. C* **2017**, *121* (11), 6218–6228.
- (15) Yakovkin, I. N.; Gutowski, M. *Surf. Sci.* **2007**, *601* (6), 1481–1488.
- (16) Woodward, P. M.; Sleight, A. W.; Vogt, T. *J. Solid State Chem.* **1997**, *131* (1), 9–17.
- (17) Li, M.; Altman, E. ; Posadas, A.; Ahn, C. . *Surf. Sci.* **2003**, *542* (1–2), 22–32.
- (18) Wang, F.; Di Valentin, C.; Pacchioni, G. *J. Phys. Chem. C* **2012**, *116* (19), 10672–10679.